Zeitschrift: Helvetica Physica Acta

Band: 69 (1996)

Heft: Sep. 2

Vereinsnachrichten: Réunion d'automne de la Société Suisse de Physique = Herbsttagung der Schweizerischen Physikalischen Gesellschaft = Autumn meeting of the Swiss Physical Society

Autor: [s.n.]

Réunion d'Automne de la Société Suisse de Physique

Herbsttagung der Schweizerischen Physikalischen Gesellschaft

Autumn Meeting of the Swiss Physical Society

October 10, 1996

Zurich, Switzerland

Helv Phys Acta
Vol. 69, Separanda 2 (1996)

0018-0238/96/0200S25-02$1.50+0.20/0

Doping dependence of the Fermi surface in the cuprates: a photoemission investigation

I. Vobornik, S. La Rosa, F. Zwick, H. Berger, M. Grioni,
G. Margaritondo,
R.J. Kelley*, J. Ma*, A. Chubukov*, M. Onellion*

Institut de Physique Appliquée, DP, EPFL, CH-1015 Lausanne
*Department of Physics, University of Wisconsim, Madison, WI 53706

We have exploited angle-resolved photoelectron spectroscopy (ARPES) to study the electronic structure of single crystal samples of high T_C material $Bi_2Sr_2CaCu_2O_{8+\delta}$ and of the antiferromagnetic insulator $Sr_2CuO_2Cl_2$. As one moves away from optimal doping into underdoped region (T_C as low as 30K), the large Fermi surface sheet centered around the (π,π) point evolves into a small pocket centered around $(\pi/2,\pi/2)$, and the saddle-point van Hove singularity is lost. This evolution can be extrapolated to $Sr_2CuO_2Cl_2$, which is apparently well described by the mean field spin-density wave calculation.

We have performed angle resolved photoemission (ARPES) study of electronic structure of the underdoped superconducting BSCCO-2212 (T_C~60K, T_C~30K) and insulating $Sr_2CuO_2Cl_2$ single crystals. The materials involved represent three steps in evolution from an antiferromagnetic insulator to an optimally doped superconductor, and therefore, this study reveals some points of the evolution process of the electronic band structure with doping.

The experiment has been done in the Synchrotron Radiation Center in Madison, Wisconsin, at the NIM-4 beamline. Clean sample surfaces have been obtained by cleaving *in situ*, at a base pressure better then 10^{-10}mbar. The high symmetry directions in the Brillouin zone have been determined by low energy electron diffraction. Photoemission measurements have been carried out with a 50mm electrostatic hemispherical analyzer, mounted on a two-axis goniometer, providing angular resolution < 2°. The total energy resolution was 30 meV.

BSCCO-2212 and $Sr_2CuO_2Cl_2$ have isostructural CuO_2 planes. In our photoemission measurements we have followed the high symmetry directions Γ–M$(0,\pi)$ and Γ–Y$(\pi,-\pi)$, and, additionally, the lines parallel to Γ–Y and Γ–X(π,π), in order to determine Fermi surfaces of the superconducting samples

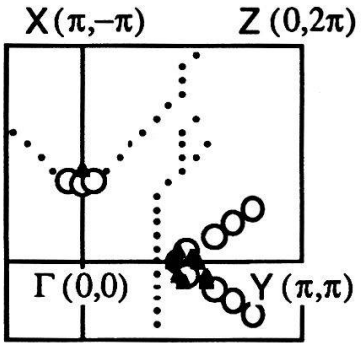

Fermi surface
• optimally doped
O underdoped, $T_C \approx 60$ K
▲ underdoped, $T_C \approx 30$ K

Fig. 1)

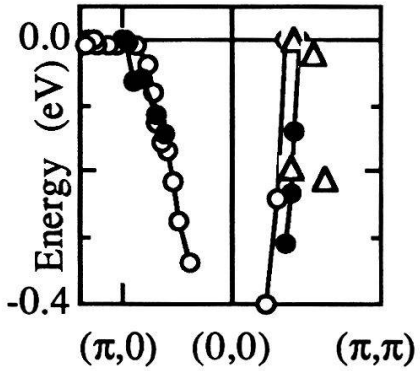

—●— BSCCO-2212, $T_C \approx 60$ K
—△— BSCCO-2212, $T_C \approx 30$ K
—○— BSCCO-2212, $T_C \approx 95$ K

Fig. 2)

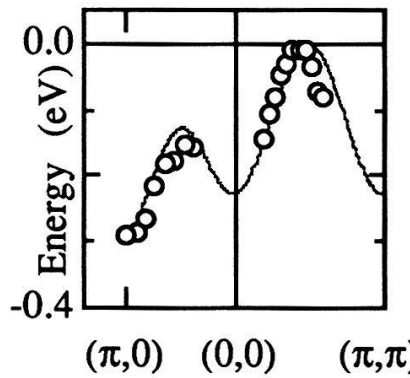

o $Sr_2CuO_2Cl_2$
— Mean-field SDW calculation

Fig. 3)

The results extracted from the photoemission spectra are presented in the figures 1), 2) and 3). Fig. 1) exhibits Fermi surfaces of the three differently doped BSCCO-2212 with critical temperatures of 92 (optimal doping), 60 and 30 K. The large sheet of the Fermi surface, centered around Y in the case of optimal doping, shrinks with reduction in doping and becomes ~3 times smaller for the T_C~60K sample. With further doping reduction, T_C~30K sample, Fermi surface shrinks to a small pocket centered around $(\pi/2,\pi/2)$ [1].

Figures 2) and 3) present energy dispersion for superconducting and insulating samples respectively. Several important features should be noticed: the flat band (van Hove singularity), present in the case of optimal doping in Γ–M, disappears with reduced doping (T_C~60K sample) [1]. $Sr_2CuO_2Cl_2$ is well described by the mean field spin-density wave calculation, taking into account the next nearest neighbour hopping interaction (J=130 meV, t'=-73 meV) [2-4]. BSCCO-2212;T_C~30K and $Sr_2CuO_2Cl_2$ posses the same type of dispersion, with the E(k) maximum, placed at the $(\pi/2,\pi/2)$ point. This indicates the precursors of the antiferromagnetic correlations in sufficiently underdoped superconductors.

1. S. La Rosa et al., to be published
2. A. Kampff and J.R. Schrieffer, Phys.Rev.B 42 (1990) 7967
3. D. Duffy and A. Moreo, Phys.Rev.B 52 (1995) 15607
4. A. Chubukov and K. Muselian J.Phys.Cond.Matt. 7 (1995) 133

Helv Phys Acta
Vol. 69, Separanda 2 (1996)

0018-0238/96/0200S27-02$1.50+0.20/0

ON THE GEOMETRICAL BARRIER IN TYPE I SUPERCONDUCTORS

H. Castro and L. Rinderer

Institut de Physique Expérimentale, Université de Lausanne, CH-1015 Lausanne, Switzerland

ABSTRACT

The magneto-optical technique was used to study the edge barrier in type I superconducting strips. We measured the flux-free zones in the sample edges and its dependence on the field magnitude and temperature. Standard I-V measurements allowed us to study the critical current originated by the edge barrier in these pinning-free samples. Our results show the predominant role of the geometrical edge barrier.

INTRODUCTION

A calculation of the current and field distributions [1] in superconducting strips with sharp edges shows that Meissner currents occupy the whole sample at low fields. As the applied field increases, magnetic flux starts to fill the central part of the strip leaving two flux-free zones at the edges. The width of these zones decrease as the applied field increases. Meissner currents circulate only inside these flux-free zones. The distribution of currents produces a geometry-related barrier for the penetration and movement of normal domains. The edge barrier give rise to an enhancement of the critical current or its appearance, in pinning-free samples [2]. There is, however, disagreement among different authors on the role played by different possible edge barriers like the Bean-Livingston, Gibbs free-energy and the geometrical one, in the observed regimes of vortex motion in high-T_c superconductors, which can be attributed either to bulk pinning or to any of these barriers [1, 3]. Therefore we decided to study the properties of the geometrical barrier in the simple case of pinning-free type I superconductors. Hereafter we present preliminary results of this study.

RESULTS AND DISCUSSION

Figure 1 shows a sequence of magneto-optical images at different fields, where the flux-free zone can be clearly seen as a dark strip to the right side of the images. The field dependence of the flux-free zone width ΔX is plotted in Fig. 2, where $h = H/H_c$. The experimental points in Fig. 2 are in good agreement with the solid line, which represents the equation

$$\Delta X(h) / L_x = 1 - \sqrt{1 - (2L_y / L_x \cdot \frac{1}{h})^2} \qquad (1),$$

obtained from reference 1 by replacing H_{c1} by H_c ($\approx$ 220 Oe) in the expression for H_p. The thickness to width ratio L_y/L_x is 0.067 for this sample.

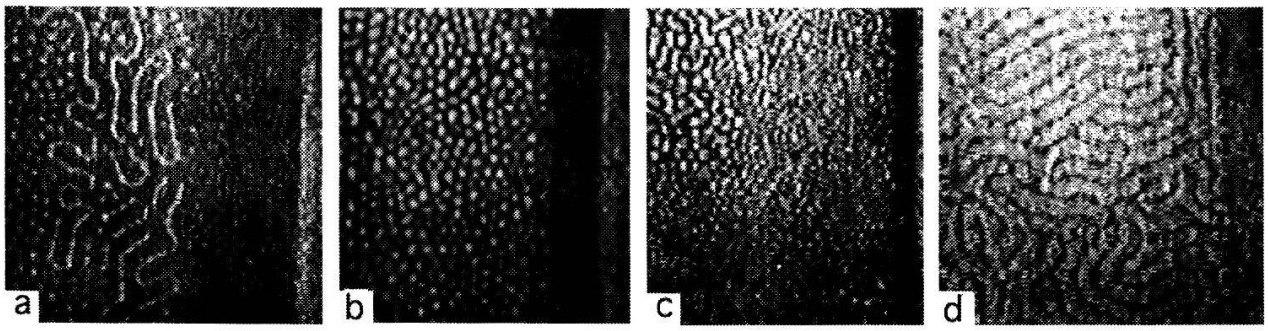

Fig. 1 Magneto-optical images (only right half of sample is shown), illustrating the flux-free zone at different fields for an In sample at 1.7 K. Applied fields: a- 45 Oe, b- 66 Oe, c- 89 Oe, d- 178 Oe

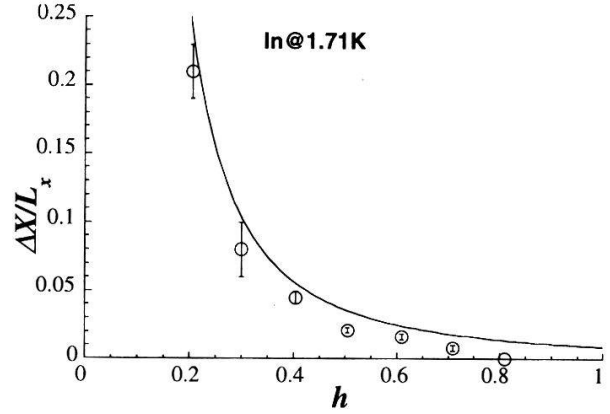

Fig. 2 Field dependence of ΔX for Indium

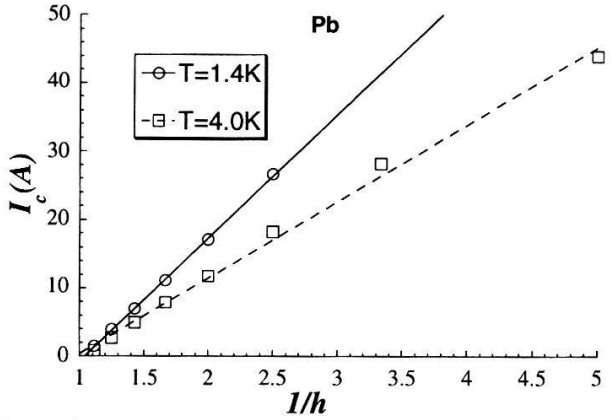

Fig. 3 Critical current vs. inverse of reduced field

The critical current was determined with the four probe dc-method as discussed by Dutoit [4]. Fig. 3 presents the field dependence of I_c for a Pb sample at two different temperatures. All the measured samples were found to satisfy the following equation [4],

$$I_c(h,T) = I^*(T)\cdot(1/h - 1) \qquad (2).$$

The parameter $I^*(T)$ is determined by the sample type and geometry. A remarkable feature in the I-V curves is that the extrapolated lines intercept, with a good precision, at the point $(-I^*, -R_nI^*)$, where R_n is the sample's resistance for h=1. Fig. 4 shows the dependence of I_c on sample thickness L_y, and Fig. 5 the temperature dependence of I_c. both dependencies are linear.

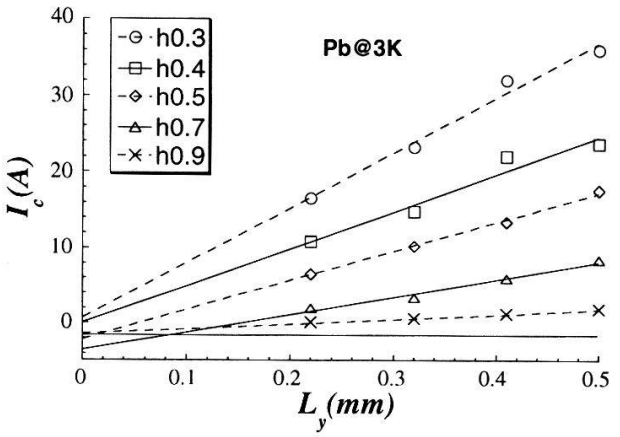

Fig. 4 I_c vs. sample thickness for Pb at 3K

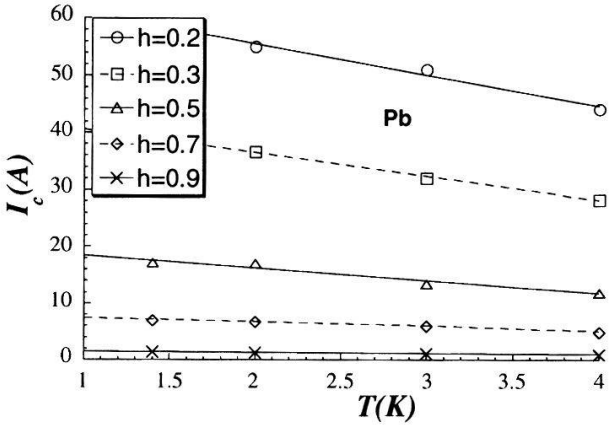

Fig. 5 I_c vs. temperature for Pb

CONCLUSIONS

Our experimental results confirm the field dependence of the flux-free gap proposed in ref. [1]. The critical current originated from the geometrical barrier was studied and its dependence on field, sample thickness and temperature was presented. We believe that further theoretical and experimental work is needed to complete the understanding of the edge barrier.

We thanks Dr. I. L. Landau for fruitful discussions. The present data is a re-analysis of the data measured by Dr. B. Dutoit [4]. This work was partially supported by the Swiss National Science Foundation.

REFERENCES

[1] E. Zeldov et al., *Phys. Rev. Lett.* **73** (1994)1428
[2] J. R. Clem, *J. Low Temp. Phys.* **12** (1973) 449
[3] L. Burlachkov, *Phys. Rev. B* **47** (1993) 8056; D. Chen et al., *Phys. Rev. B* **48** (1993) 6426
[4] B. Dutoit, PhD thesis IPE- Lausanne University 1992

Helv Phys Acta
Vol. 69, Separanda 2 (1996)

0018-0238/96/0200S29-02$1.50+0.20/0

Influence of Substrate Type on the Properties of BISCCO Thin Films

A. Mariño[1], F. Ichikawa[2] and L. Rinderer

Institut de Physique Expérimentale, Université de Lausanne, Switzerland

Highly oriented $(Bi_{0.8}Pb_{0.2})_2Sr_2Ca_2Cu_3O_{10+\delta}$ thin films were prepared by rf magnetoron sputtering on (100) MgO, $SrTiO_3$ and $LaAlO_3$ substrates. Deposited films were post-annealed at the same temperature for different annealing times. The influence of the substrate type and annealing duration on T_c and J_c, structure and surface morphology is reported.

Introduction: It is known that the granular character of the high T_c oxides, due to the short coherence length, has profound influence on their superconducting properties. Specially the critical current density (J_c) is strongly limited by grain boundaries [1]. We present here results of resistivity (ρ), J_c and crystalline structure as determined by XRD of $(Bi_{0.8}Pb_{0.2})_2Sr_2Ca_2Cu_3O_{10+\delta}$ (BISCCO) thin films and discuss the influence of substrate type and thermal processes.

Experimental: Highly c-axis oriented BISCCO thin films were produced by OFF-AXIS rf magnetron sputtering on polished (100) MgO, $SrTiO_3$ (STO) and $LaAlO_3$ (LAL) single crystals. A single target with different nominal composition was used [2]. The films deposited at about 600°C were thereafter annealed in air at different temperatures during different times, together with a sintered ceramic.

Results and Discussion: The temperature dependent resistivity $\rho(T)$ for films deposited

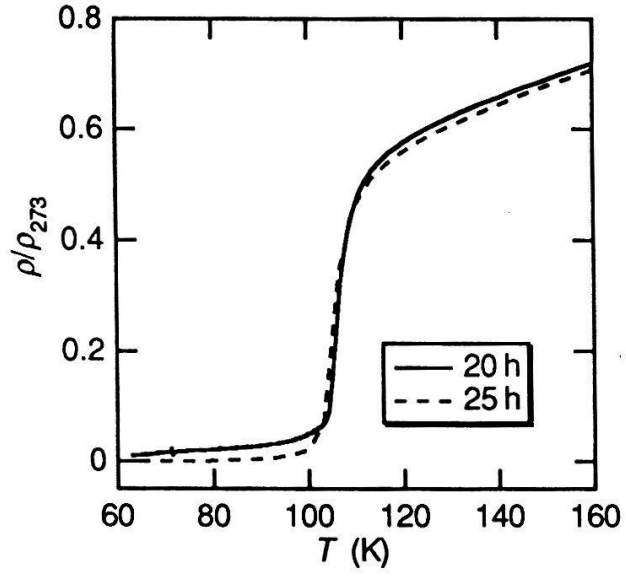

Figure 1: Normalized resistivity vs T of BISCCO/MgO thin films for different annealing times: 20 h and 25 h.

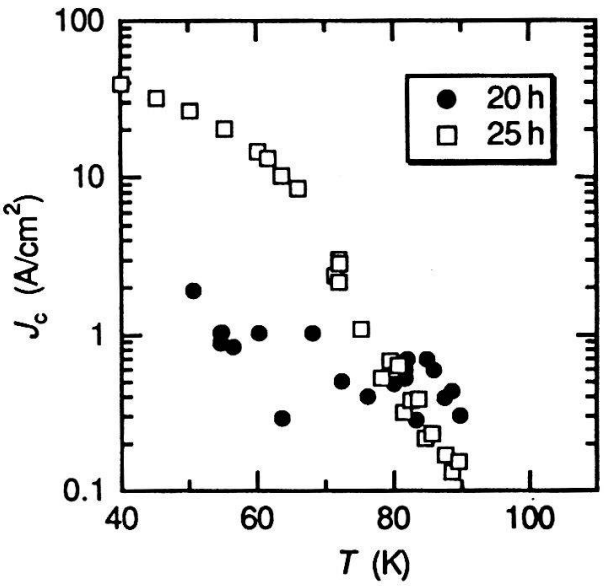

Figure 2: Critical current density vs T of BISCCO/MgO thin films for 20 h and 25 h annealing time.

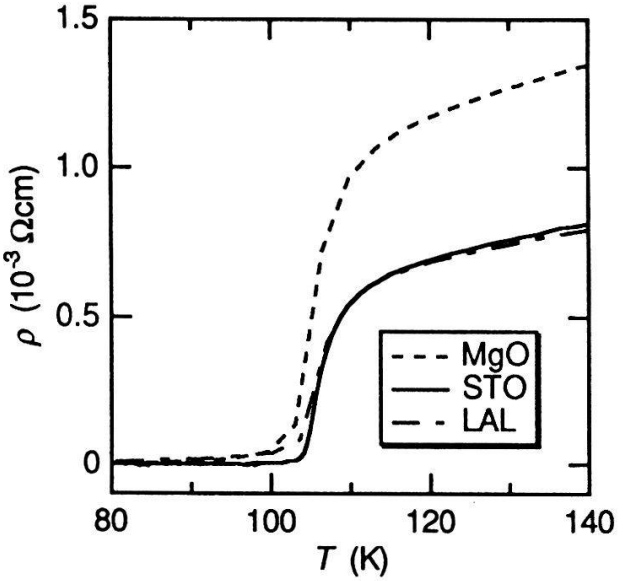

Figure 3: ρ vs T curves of BISCCO nearly single phase samples on MgO, STO and LAL substrates. Annealing time: 25 h for MgO and STO, 20 h for LAL.

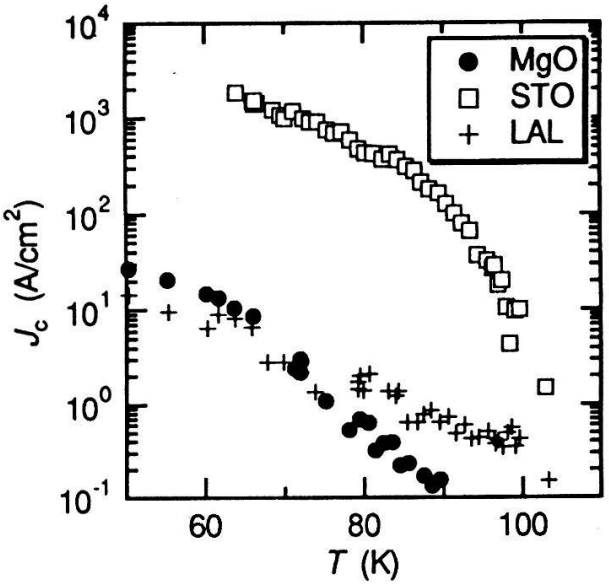

Figure 4: The corresponding J_c vs T curves of BISCCO thin films on MgO, STO and LAL substrates.

on MgO at different annealing times are shown in Fig. 1. By increasing annealing time, both the residual resistivity (ρ_0) and the transition width become smaller. Similar behavior was observed for BISCCO/STO films and can be associated with an increase of the high temperature phase (H-BISCCO), as confirmed with XRD analysis. A different behavior, an increasing of the low temperature phase (L-BISCCO) with increasing annealing time, was observed in BISCCO/LAL samples. Figure 2 displays the $J_c(T)$ curves for BISCCO/MgO films. The highest J_c values ~ 1 A/cm^2 at 77 K are obtained in samples annealed 25 h, where both H-BISCCO phase become predominant and crystalline grains grow larger [2]. Figure 3 shows the $\rho(T)$ curves for nearly single phase samples on different substrates. It is observed that for BISCCO/STO films the transition width become smaller than for BISCCO/MgO and BISCCO/LAL films. The corresponding J_c vs T curves are shown in Fig. 4. For all the samples the temperature behavior of J_c depends on the substrate type. Furthermore an enhancement of the critical current density larger than two orders of magnitude, was observed in BISCCO/STO films ($J_c \sim 700$ A/cm^2 at 77 K). Texture effects can considerably improve J_c, however, pinning effects produced by the presence of L-BISCCO phase can not be ruled out [3].

References

[1] G. Deutscher, *Earlier and Recent Aspects of Superconductivity.* J.G. Bednorz and K.A. Müller (Eds.) (Springer-Verlag, 1990).

[2] A. Mariño, T. Yasuda, E. Holguin and L. Rinderer, Physica C **210**, 16 (1993).

[3] H. Rodriguez, H. Sáchez and A. Mariño, *Proceeding of the 21st International Conference on Low Temperature Physics,* Czechoslovak Journal of Physics, **46** Suppl. S3 (1996) 1703.

[1] On leave from Dept. of Physics, Universidad Nacional de Colombia, Bogota, Colombia.

[2] On leave from Dept. of Physics, Kyushu University, Fukuoka, Japan.

Helv Phys Acta
Vol. 69, Separanda 2 (1996)

0018-0238/96/0200S31-02$1.50+0.20/0

On the Reproducibility of the Resistive Transition Anomalies in Superconducting Nanostructures

K. Yu. Arutyunov[1,2], S. V. Lotkhov[1], A. B. Pavolotski[1], D. E. Presnov[1] and L. Rinderer[2]

[1] Moscow State University, Physics Faculty, 119899, Moscow, Russia
[2] Université de Lausanne, Institut de Physique Expérimentale, CH-1015, Lausanne, Switzerland

Four contact R(T) measurements have been performed for various multi-probe aluminium nanostructures. For several samples (combinations of probes) the resistance at the top of superconducting transition can increase the corresponding normal state value. The effect is not fully reproducible, being dependent upon cooling history and particular arrangement of voltage and current probes. While the resistive transition, the inevitably formed normal - superconducting boundary is considered to be responsible for the observed anomaly due to additional voltage step at the N/S interface. The absence of full reproducibility of experimental results is attributed to the dramatic sensitivity of mesoscopic-size samples transport properties on the variation of boundary (scattering) conditions.

In a number of recent publications [1] it was reported that for superconducting nanostructures the resistance at the top of superconducting transition can exceed its normal state value R_N. Several models [1-3] were proposed to describe the origin of this phenomenon.

In the present paper we present results of experimental study on various aluminum nanostructures. The R(T) characteristics have been measured for several multi-probe aluminum nanostructures with the line width <100 nm using conventional 4-contact technique. We did observe that for the majority of samples (combinations of current and voltage probes) the R(T) dependencies display conventional monotonous behavior, while for several combinations of contacts there can be pronounced increases of the resistance at the top of superconducting transition (Fig.1). The existence of the resistive 'bump' depends upon the history of the sample cooling and could be sometimes eliminated by heating up to ~15 K (Fig.2).

It was proposed [2-3] that while the resistive transition the inevitably formed normal - superconducting boundary is responsible for the observed anomaly due to the additional voltage step at the N/S interface [4]. For the normalized excess resistance it is easy to obtain:

$$\frac{\Delta R_{N/S}}{R_N(T)} = \frac{R(T) - R_0(T)}{R_N(T)} = \frac{\Lambda(T)Z(T)}{L} \qquad (1),$$

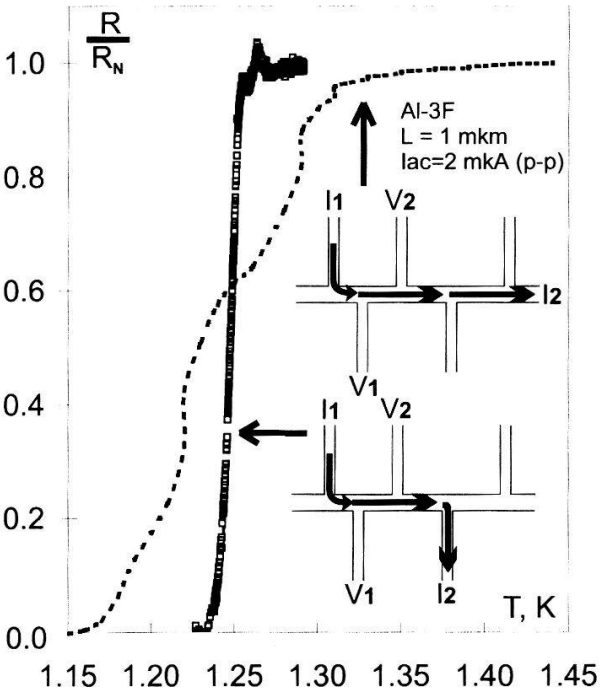

Figure 1. R(T) dependencies for the same sample Al-3F and the same arrangement of voltage probes, but for different current contacts configuration.

where L is the sample length (the distance between voltage probes) and $\Lambda(T)$ is the characteristic quasiparticle relaxation length. For most thin film nanostructures the 'dirty limit' approximation ($l << \zeta_0$) is suitable: $\Lambda = (l\zeta_0)^{1/2}$, where ζ_0 is the BCS coherence length and l is an electron mean free path. Z(T) function incorporates the probability of the quasiparticles not being Andreev reflected at the N/S boundary, and sufficiently close to the critical temperature $Z(T_C) \sim 1$. $R_0(T)$ describes the 'original' form of the resistive transition if there were no any N/S interface(s). Unfortunately, the $R_0(T)$ function could be hardly calculated from the 'first principles' for the actually used rather inhomogeneous lithographically prepared thin film structures. However, in any case, for the proposed origin of the resistive 'bump' the actual R(T) curve should be vertically shifted by $\Delta R_{N/S}$ relatively to $R_0(T)$ (Fig.3). Here it should be noticed that it is absolutely unnecessary that the N/S interface should be always perpendicular to the sample axis. The tilting (or random deformation) of the N/S boundary will cause the redistribution of the current across the wire (Fig. 3b and 3c),while the

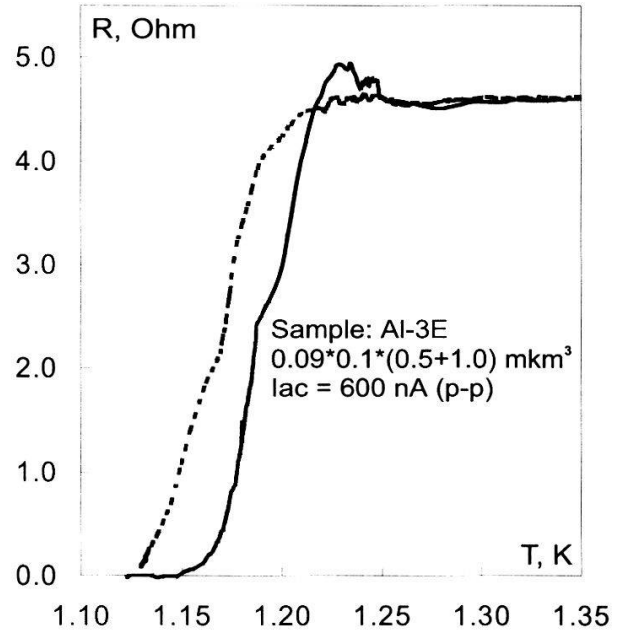

Figure 2. R(T) dependencies for the same sample Al-3E recorded with the time interval of 3.5 hours after heating up to ~15 K.

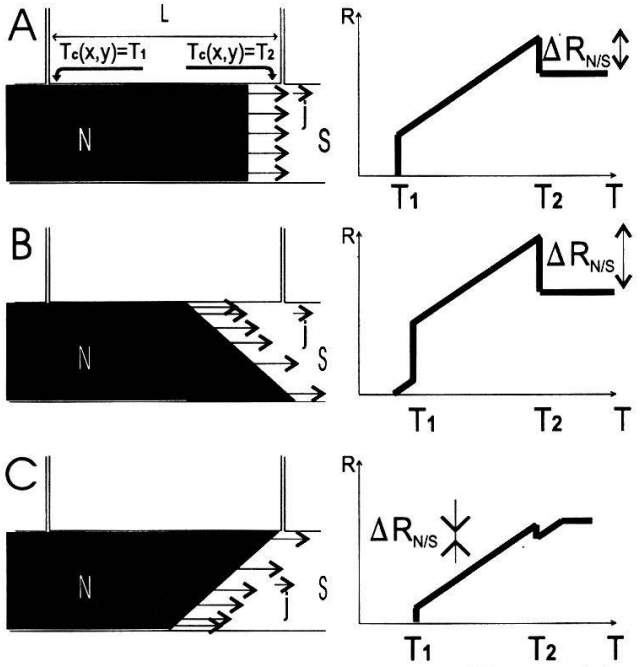

Figure 3. Scematic explanation of origin of the different resistive 'bump' magnitudes in case of various forms of the N/S interfaces while the spreading of the N(S) domain. Linear form for the R(T) function is selected for simplicity.

voltage measured by the potential contacts is proportional to the local current density within the locus of the probes. This explains relatively random variation of the discussed anomaly magnitude (position of the resistive 'bump' on the $R_0(T)$ dependence) from sample to sample. The studied nanostructures are small enough to show well-known mesoscopic effect: changing of normal state scattering pattern due to displacement of a few impurity atoms. This effect could explain the bad reproducibility of results and dependence on cooling history due to the variation of the conditions of the N(S) phase nucleation (Fig.2).

Notice that for practically used nanostructures the width of the contacts is comparable to the width (or even the length) of the 'body' of the sample. Thus, the existence of voltage probes could not be considered as a 'small perturbation', and the details of the N/S boundary propagation within the locus of contacts are difficult to be predicted. However, it is obvious that the magnitude of the resistance anomaly (the position of the 'bump' on the $R_0(T)$ curve) is dramatically dependent upon these details. Changing of the contacts configuration for the given nanostructure drastically influence the form of the resistive transition (Fig.1).

If to consider extremely homogeneous 1D objects, it should be mentioned that in this case the origin of the resistive transition could be described by the model of thermal activation of phase-slip centers [5]. Contrary to the discussed above static model, the N/S interfaces in the last case are periodically established with the frequency of thermal fluctuations Γ and are healing during the characteristic quasiparticle relaxation time τ_{Q^*}. For such a dynamic description the purely static equation (Eq.1) should be used with corresponding time averaging [1]. However, while the dynamic resistive state model differs significantly from the static one, all the considerations about the reproducibility of experimental results are still qualitatively valid as the formation of phase-slip center(s) is also strongly dependent upon the sample inhomogeneity.

Thus, in conclusion we may state that the small size of superconducting nanostructures is responsible for the random observation of the resistance 'bump', the 'bad statistics', probable significant magnitude of the effect in comparison with macroscopic objects ($L>>\Lambda$), and not for the origin of the anomaly itself.

The authors want to acknowledge Dr. I. L. Landau for pointing their attention to the N/S boundary problem and for permanent valuable discussions. The work was supported by the Russian Fund for Basic Research 95-02-04151A.

References

[1] K. Yu. Arutyunov, Physical Review B, **53**, 12304 (1996), and the references there.
[2] I. L. Landau, private communication.
[3] K. Yu. Arutyunov *et al.*, Czechoslovak J. of Phys. **46**, 2309 (1996), Suppl. S4.
[4] A. B. Pippard, F.R.S., J. G. Shepherd and D. A. Tindall, Proceeding Royal Society, London, **A324**, 17 (1971).
[5] J. S. Langer and V. Ambegaokar, Physical Review, **164**, 498 (1967).

Helv Phys Acta
Vol. 69, Separanda 2 (1996)

0018-0238/96/0200S33-02$1.50+0.20/0

Fermi Surface of $Sn_{0.8}In_{0.2}$ by Compton Scattering

A.A. Manuel[1], D. Vasumathi[1], A. Shukla[2], P. Suortti[2], A.Yu Rumiantsev[3] and A.S. Ivanov[3]

[1]Department of Physics, University of Geneva, CH-1211 Geneva 4, Switzerland
[2]ESRF, BP 220, F-38043 Grenoble, France
[3]Russian Reserach Center Kurchatov Institute, Moscow 123182, Russian Federation

We present measurements of high resolution directional Compton profile performed on a single crystal of $Sn_{0.8}In_{0.2}$. We have determined the Fermi momentum k_F in the [100] direction . We compare the result with those obtained by positron 2D-ACAR and neutron diffraction Kohn anomaly measurements.

γ-Sn is a Sn-rich solid solution phase of the alloy Sn_xIn_{1-x}. It has a simple hexagonal structure and one atom per unit cell. The Fermi surface is therefore nearly spherical, except for small deformations where it crosses the Brillouin zone boundaries. Recently, positron annihilation 2D-ACAR measurements have been reported [1] on $Sn_{0.8}In_{0.2}$ and the position of the Fermi momentum has been determined in several crystallographic directions. Surprisingly, these values are 3-5% larger than those obtained from measurements of the Kohn anomaly in neutron scattering dispersion curves [2]. For example, in the [100] direction, i.e. along the Γ-M line of the Brillouin zone, the value of the Fermi radius k_F obtained from 2D-ACAR is 0.862 ± 0.005 a.u. while Kohn anomaly gives 0.834 ± 0.008 a.u. The origin of this difference is unclear. Various possibilities have been mentioned [1] like a) the preferential affinity of the positron for Sn-rich regions of the sample (if the sample has an inhomogeneous stochiometry) and b) an intrinsic difference between the Kohn anomaly (a ground state property) and positron annihilation (which, due to the positron-electron correlations, probes an excited state). The value of k_F obtained from band structure calculations [1] is 0.852 a.u. This intermediate value does not provide a satisfactory explanation of the two measurements. Therfore, we have thought a third independant measurement of k_F. As the traditional electron cyclotronic methods fail in alloys because of the electronic mean free path being too small, we have turned to Compton profile measurements.

We have used the high resolution Compton spectrometer at ID 15 at ESRF [3] with a monochromatic photon beam of 57.8 keV. This large energy is needed to investigate γ-Sn, a material with a large atomic number and a high density. In these conditions, the resolution of the spectrometer was 0.18 a.u., providing a clear definition of the Fermi edge. Figure 1 shows the result of this experiment performed in the [100] crystallographic direction with the single crystal sample already used for neutron and positron measurements. The data points have been corrected for absorption in the sample, the detector, the air and the Mo filter used to suppress fluorescence lines around the Compton profile.

To analyse the experimental profile, a broad component described by a polynomial of degree 3 has first been fitted above the Fermi edge ($\mid p_z \mid \geq 1.2$ a.u.). It is shown by the dashed line in Fig. 1. The contribution of the valence electrons has then been described by an inverted parabola, as expected for free electrons. This simple model agrees with the

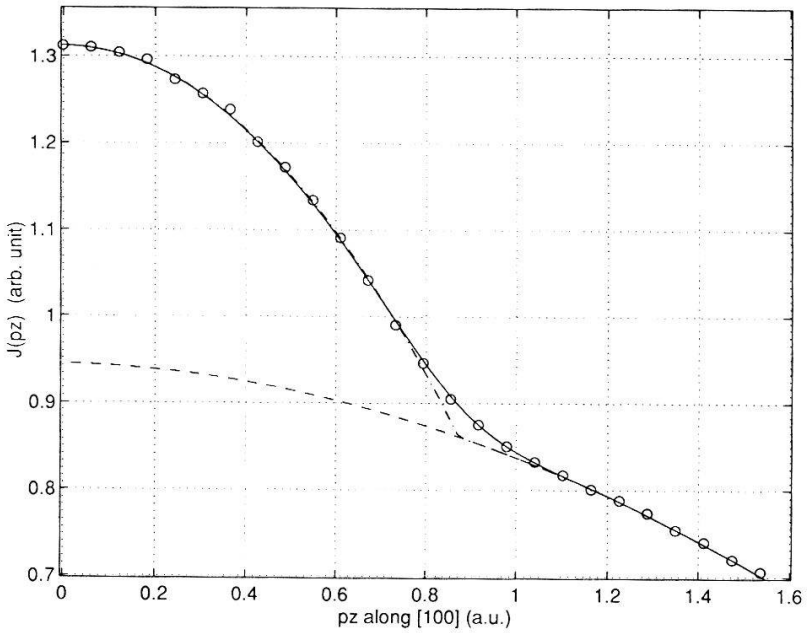

Figure 1: Measured and fitted Compton profiles of γ-Sn.

Compton profile obtained from the band structure calculations [1]. The two free parameters of the parabola (amplitude and width) have been fitted to the measurement in a momentum range limited to $\mid p_z \mid \leq 0.7$ a.u. The result is shown by the dashed-dotted line in Fig.1. The value obtained for k_F is 0.867 ± 0.01 a.u. It is slightly larger than the positron value, but we think that this small difference is not significant. We conclude that positron and Compton experiements provide the same k_F in the [100] direction.

The solid line in Fig. 1 is the sum of the two components, convoluted with a gaussian function of 0.27 a.u. This model describes well the experiemental Compton profile, in particular around the Fermi break. We notice that the smearing observed at k_F is larger than the experimental resolution would imply. This trend is similar to what has been observed for Li [4] but in this last case the smearing, attributed to electron correlations, was even larger.

We are very grateful to T. Bulaps and V. Honkimaki for their help and advices during the measurements.

References

[1] L. Hoffmann, B. Barbiellini, A.A. Manuel, M. Peter, A. Yu. Rumiantsev, and A.S. Ivanov, Physica B **222**, 31 (1996).

[2] A.S. Ivanov, A. Yu. Rumiantsev, B. Dorner, N.L. Mitrofanov and V.V. Pushkarev, J. Phys. F **17**, 1925 (1987).

[3] C. Blass, J. Redinger, S. Manninen V. Honkimaki, K. Hamalainen and P. Suorrti, Phys. Rev. Lett. **75**, 1984 (1995).

[4] Y. Sakurai, Y. Tanaka, A. Bansil, S. Kaprzyk, A.T. Stewart, Y. Nagashima, T. Hyodo, S. Nanao, H. Kawata and N. Shiotani, Phys. Rev. Lett. **74**, 2252 (1995).

Helv Phys Acta
Vol. 69, Separanda 2 (1996)

0018-0238/96/0200S35-02$1.50+0.20/0

Spectromicroscopy Study of Lateral Band Bending of the Ge-GaSe Heterostructure

J. Almeida[a], I. Vobornik[a], H. Berger[a], M. Kiskinova[b], A. Kolmakov[b], M. Marsi[b], and G. Margaritondo[a,b]

(a) Institut de Physique Appliquée, Ecole Polytechnique Fédérale de Lausanne, CH-1015 Ecublens, Lausanne, Switzerland;

(b) Sincrotrone di Trieste SpA, Padriciano 99, 34012 Trieste, Italy.

We report a study of the lateral band bending at the Ge-GaSe interface. Spectromicroscopy measurements with synchrotron radiation were performed at the ESCA microscopy line of ELETTRA in Ge patterned films on GaSe substrates. Preliminary results of lateral band bending, chemical reactions and the beam stimulated Ge surface migration are presented. These studies allowed us to seek on the microscopical equivalent of the semiconductor Debye length and to probe the capabilities of scanning-focused spectromicroscopical systems.

We present a spectromicroscopical study of the lateral band bending at the near-edge region of a patterned Ge films on GaSe substrates. Nowadays, as semiconductor devices become smaller, the new sized devices are controlled by strong size-related effects: the boundaries coupling of contacts, interfaces and surfaces. Particularly important for devices are the lateral potential variations. Space charge layers are almost always associated with interfaces.[1] Normally, it is assumed that these space charge layers have abrupt edges, but transport processes do not allow a step-like lateral profile of the carrier concentration and the space charge is usually spread over the semiconductor Debye length.

The choice of GaSe offered a layered structure simplifying relatively theory and experiment.[2] As a result of its lamellar structure, cleavage is easy, yielding step-free flat surfaces. As no chemical bonds are broken, no band gap dangling bonds surface states exist and the surface is extremely inert. The Ge-GaSe heterojunction has been considered for a long time of an "ideal Schottky-like" type.[3] The interface formation lead to a large energy shift (≈0.65 eV) of the photoemission spectral features, and finally the band bending and the valence band discontinuity reaches a saturation value for about 1.5 ML thick of Ge.

The experiments were performed on the ESCA microscopy beamline of the ELETTRA light source using a spherical grating monochromator and a 100 mm hemispherical analyzer mounted at 70 degrees with respect to the sample and normal to the incident photon beam. In the scanning photoelectron microscope, the incident photon beam was demagnified to a 0.15×0.15 μm spot by a zone plate optical system. Photoemission spectra were taken on selected points along a straight line perpendicular to the patterned Ge overlayer, by rastering the sample with respect to the focused beam. The crystals were p-type GaSe $\approx 1\times10^{14}$ cm^{-3} doped with 0.1% As. For this carrier concentration the Debye length screening was estimated to be 1 μm, much larger than the photoelectron escape depth. The samples were cleaved in-situ at a base pressure of 2×10^{-10} torr, and a nominal 4 ML thick Ge overlayer was evaporated, while keeping covered one part of the freshly cleaved surface with a sharp-edged metal screen.

Figure 1 shows a scanning photoemission image and cross-section of cleaved GaSe covered with ≈4 ML of patterned Ge taken at 490 eV with the photoelectron analyzer tuned to the Ge3d emission. The image size is 6.4×6.4 μm and the right-side brighter emission corresponds to the Ge patterned overlayer. The Ga and Se3d core levels spectra were measured from 0.15×15 μm^2 spots areas on a straight line across Ge patches on a GaSe substrate, as showed in Fig. 1.

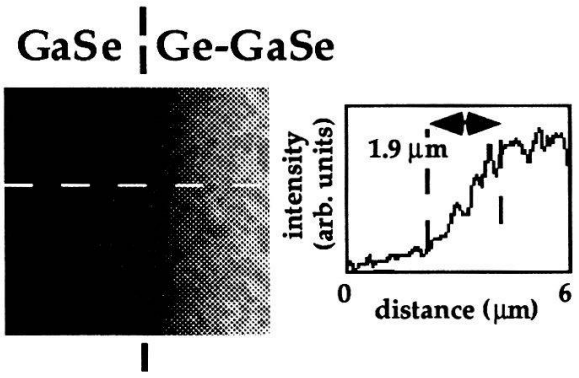

FIG. 1

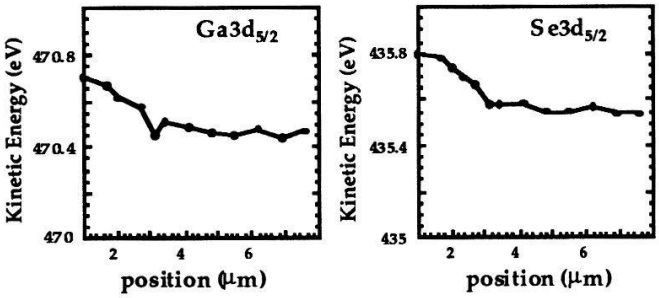

FIG. 2

The evolution of the Ga3d and Se3d core level energy positions coming from the substrate are remarkable similar, as seen in Fig. 2. The spatial differences in peak energy position from one side to an other are quite evident. Such differences shifts are equal for the two core levels, suggesting that these levels are both following the band bending. Moving from left (point x=0) to the right along the dashed line of Fig. 1, the Ga3d and Se3d bulk components themselves shift by ≈0.3 eV to lower kinetic energy along a distance of about 1.9 μm before to stabilize.

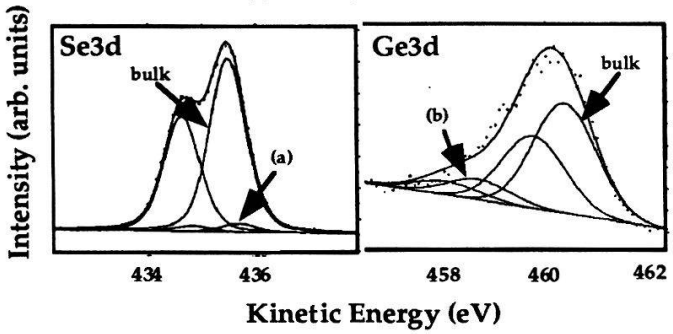

FIG. 3

On the Ge covered areas, the deconvolution best fit of the Ge3d and Se3d core levels include two components. We identified them as the bulk doublet, and the Ge-Se reacted doublet (Fig. 3, component a). The latter was shifted by 1.7 eV for Ge3d, and -0.2 eV for Se3d to lower and higher kinetic energies than the bulk doublet.

In the scanning photoelectron microscope the beam density in the submicrometer size focus spot is of 10^9-10^{10} photons/s. The evolution of the experiment showed that a prolonged exposure of the Ge overlayer drove a significant diffusion on the GaSe surface. We measured the Ge 3d core level intensity in function of time for a typical 6 ML thick overlayer. Germanium atoms released from their sites by photon stimulation and/or thermal activation diffuse isotropically across the surface. We can roughly estimate the decay considering a simple surface diffusion model. In this case, the amount of Ge atoms in the probe point is given by $N_{Ge} = N_0 - n_{Ge}\sqrt{D\,t}$. We considered the decay of the Ge3d photoelectron intensity related to surface diffusion not to substrate-overlayer chemical reactions, as shown by the core level analysis at any coverage. The linear behavior with time of the Ge photoemission intensity with a slope $n_{Ge}\sqrt{D}$ corroborates the diffusion limited character of the process.[4]

References

[1] L. J. Brillson, *"Surfaces and interfaces: Atomic-Scale Structure, Band Bending and Band Offsets"*, in *Handbook on Semiconductors*, edited by P. T. Landsberg. (North Holland, Amsterdam, 1992)

[2] G. Margaritondo, J. E. Rowe, and S. B. Christman, Phys. Rev. B. **15** , 8 (1977) 3844-3854.

[3] R. R. Daniels, G. Margaritondo, C. Quaresima, P. Perfetti, and F. Levy, J. Vac. Sci. Technol. A **3** , 3 (1985) 979-980.

[4] J. F. Nützel and G. Abstreiter, Phys. Rev. B, **53**, 20 (1996).

Helv Phys Acta
Vol. 69, Separanda 2 (1996)

0018-0238/96/0200S37-02$1.50+0.20/0

Ion Motion in Pulsed Coronas

W. Egli and U. Kogelschatz

ABB Corporate Research, 5405 Baden, Switzerland

Pulsed corona discharges are used in electrostatic precipitators with pulsed or intermittent energization. We consider the classical ESP configuration of thin round high voltage electrodes between plane grounded collecting plates. The time dependent solutions for the current and ion distributions are presented. We treat three cases in which the duration of the corona pulse is longer than, comparable to or shorter than the ion transit time from the high voltage electrode to the collecting plate. The computations show that the radial extension of the traveling annular ion cloud decreases during transit.

At atmospheric pressure the active corona region around a high voltage electrode is extremely thin. In this region the electric field surpasses the ionisation limit and positive ions are generated together with free electrons. The positive ions travel only a short distance to the negative high voltage electrode. The electrons rapidly attach to electronegative molecules and form negative ions that have to travel all the distance to the grounded collecting plates. It is this passive ion region that occupies most of the space in an electrostatic precipitator and that is responsible for particle charging and particle transport. The ions follow the electric field lines from the high voltage electrode to the collecting plates. Their velocity is proportional to the local value of the electric field. The properties of such a unipolar ion drift region can be described by the following set of equations:

$$\text{div}\,\mathbf{E} = \rho/\varepsilon\,,\ \partial\rho/\partial t + \text{div}(\rho\mu\mathbf{E}) = 0 \ \text{ and } \ \mathbf{E} = -\,\text{grad}\,\Phi \qquad (1)$$

$\mathbf{E}$ is the electric field, ρ the charge density, ε the permittivity, μ the mobility of the negative ions and Φ the potential. We use two boundary conditions for the potential: $\Phi = -U$ at the high voltage electrode and $\Phi = 0$ at the collecting plates. In addition the space charge density at the high voltage electrode is specified: $\rho(E) = c\ \bar{\alpha}$. In this relation the effective ionisation coefficient $\bar{\alpha}$ is only a function of the local value of the electric field and the unknown constant c can be determined from measured current/voltage relations in the given electrode geometry [1, 2]. As initial condition we set the space charge density equal to zero.

In this contribution we investigate the motion of the ion cloud and the average current density at the collection plate for corona pulses of different length. In the model the corona is switched by modulating the charge injection while the voltage is arbitrarily kept constant. A rather course mesh (4x40x20) is used in these 2D calculations and time steps of 50 µs are used. Fig. 1 shows the current response at the collecting plate for three different pulses of 300 µs, 3 ms and 10 ms duration. The ion transit time in this configuration (6 mm wire diameter, plates of 400 mm spacing, separation of wires: 225 mm) is about 3 ms. Fig. 2 shows two stages of the annular ion cloud of the shortest pulse. It is apparent that the radial width of the ion cloud gets smaller during transit. One of the reasons for this effect is the strongly decaying electric field from the

wire to the plate. Consequently, the ion velocity μE at the rear edge is always higher than that of the front edge. At the same time the ion density decreases along the field lines as $\rho(t)= \rho(0)/\{1 + t\,\mu\,\rho(0)/\varepsilon\}$ according to the characteristic solution of (1).

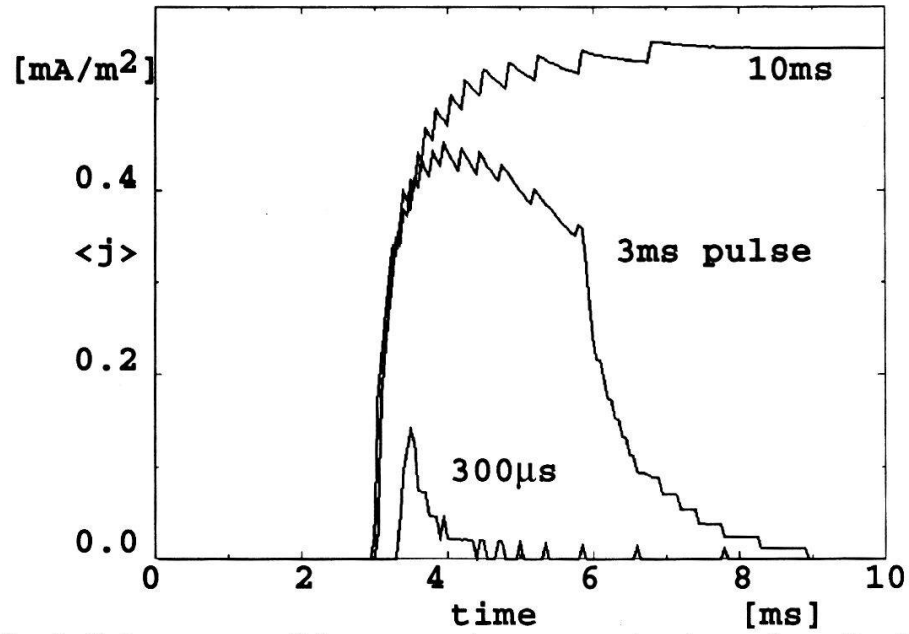

Fig. 1: Pulse answer of the average ion current density at the collecting plate for corona pulses of different duration. For the solution of (1) the method of characteristics is used for the charge and a finite element solver for the field. U=76 kV.

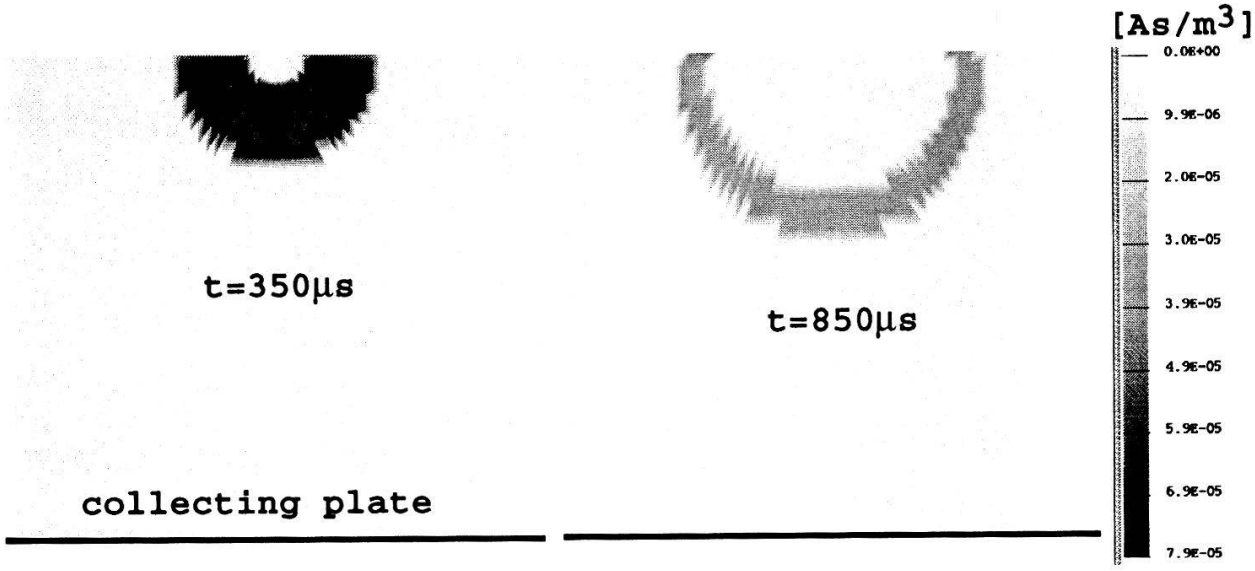

Fig. 2: Extension of the propagating ion cloud after 350 µs and 850 µs for the short 300 µs pulse. The conditions are identical to those of Fig. 1.

Intermittent energization is an important technical option for modern electrostatic precipitators. In reality the corona pulse is terminated by a reduction of the external voltage or by accumulation of space charge in the vicinity of the high voltage electrode.

References:

[1] W. Egli and U. Kogelschatz, Helv. Phys. A. **68** (1995), 203-204

[2] W. Egli and U. Kogelschatz, ICPIG XXII, Hoboken, New Jersey, 1995, Vol. **1**, 119-120

Helv Phys Acta
Vol. 69, Separanda 2 (1996)

0018-0238/96/0200S39-02$1.50+0.20/0

Magnetic field dependence of the vapor-cell Zeeman optical trap

Thomas Marty

Institute of Quantum Electronics, Eidgenössische Technische Hochschule Hönggerberg, CH-8093 Zürich, Switzerland

The number of trapped cesium atoms as function of cooling laser detuning and magnetic field gradient has been measured for the vapor-cell Zeeman optical trap and is represented by a contour map. The measured contours are compared with the predictions of a one-dimensional theoretical model of the capture process that includes the spatially varying magnetic field and was proposed by Lindquist [1]. The theoretical model tends to overestimate the detuning dependence of the number of trapped atoms.

While the magneto-optical trap is widely used to produce samples of cold atoms, a three dimensional description of the capture process is far too complicated to be solved analytically. Even for numeric computations the problem has to be considerably simplified.

Monroe *et al* [2] have shown that the number of atoms contained in the trap is determined by the balance between the capture rate R into the trap and the loss rate $\frac{1}{\tau}$ (τ =lifetime) from the trap, $\frac{dN}{dt} = R - \frac{N}{\tau}$. The dominant loss mechanisms are collisions of atoms in the trap with atoms in the vapor. For R it is assumed that all atoms with velocities less than a capture velocity v_c are slowed sufficiently after entering the intersecting laser beams, so that they are loaded into the magneto-optical trap. The models presented so far [1, 3] describe the slowing process of the atoms from the Doppler cooling viewpoint [4] and differ in the determination of the capture velocity v_c. The space dependent contribution of the scattering force is merely accounted for by a space dependent modification of the detuning in the scattering rate of the laser photons. This work checks the qualitative aspects of these models with measured data Fig. 1, by contour-maps Fig. 2, Fig. 4.

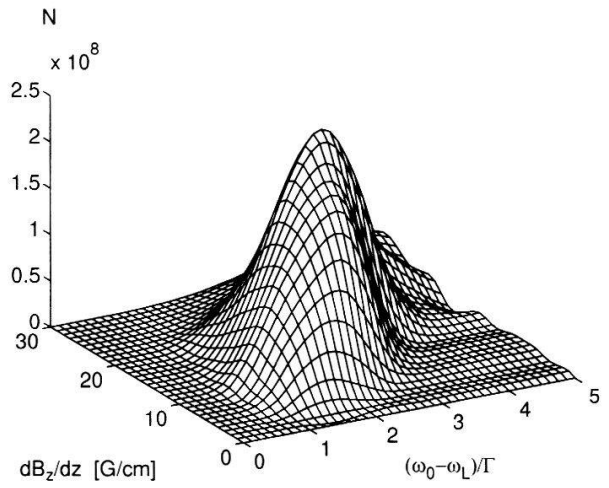

FIG. 1. Number of trapped atoms as function of the axial magnetic field gradient and cooling laser detuning. The figure is generated out of 291 measured data points at a laser intensity of 3.0 $\frac{mW}{cm^2}$ and 13 mm beam diameter. The lifetime was $\tau = 4.8\,s$.

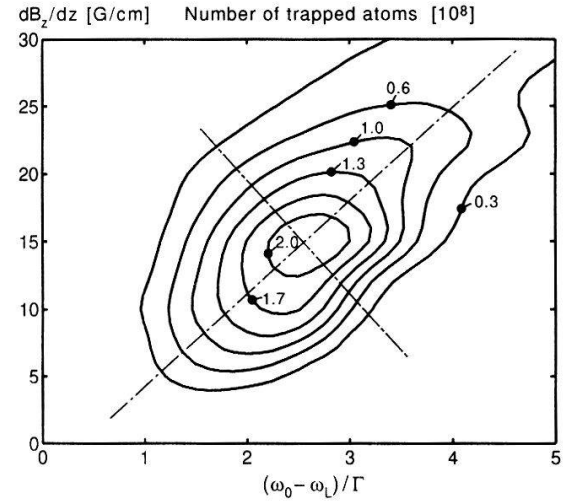

FIG. 2. Contour map constructed of Fig. 1. The maximum number of trapped atoms is measured at an axial magnetic field gradient of $15\,G/cm$ and at a cooling laser detuning $\omega_0 - \omega_L = 2.5\,\Gamma$, where $\Gamma = 2\pi \times 5\,MHz$.

The number of trapped cesium atoms was determined by fluorescence measurements. A fraction of 1/165 of the total fluorescence was imaged by a lens on a detector. To calculate the number of trapped atoms, the cloud was assumed optical thin and the atoms were approximated by two-level systems. Therefore the transition strength of the $|4\,4\rangle \rightarrow |5\,5\rangle$ cycling transition was used, $I_s = 2.2\,\frac{mW}{cm^2}$. To get the detuning and magnetic field dependence, the fluorescence was sampled on a net of 291 nodes Fig. 1, and represented by a contour-map, Fig. 2.

The measured data is compared with a theoretical model that includes the spatially varying magnetic field in the trap Fig. 3, and was proposed by Lindquist [2]. The calculated contours of equal number of atoms, Fig. 4, show a much stronger decrease with increasing cooling laser detuning than is experimentally observed. The steep decrease is a characteristic feature of theoretical models that assume independent scattering rates of the cooling laser beams. Moreover theoretical models that describe the slowing of the atoms, but not the capturing, predict captured atoms at zero magnetic field gradient, though at well aligned trap, there is no space dependent force that compensates for gravity. In general it is critical to predict precisely the conditions for the maximum number of atoms. Moreover the theoretical model tends to overestimate the detuning dependence of the number of trapped atoms.

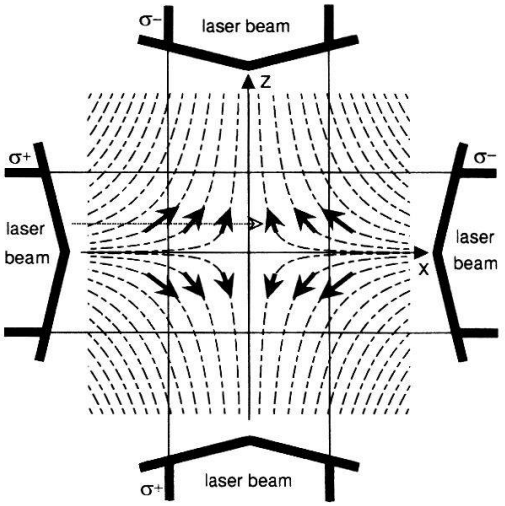

FIG. 3. The anti Helmholtz coils produce a spatially varying magnetic field in the trap. For an atom moving displaced from the axis the circular polarised laser beams drive $\Delta m = 0, \pm 1$ transitions in the basis defined by the magnetic field.

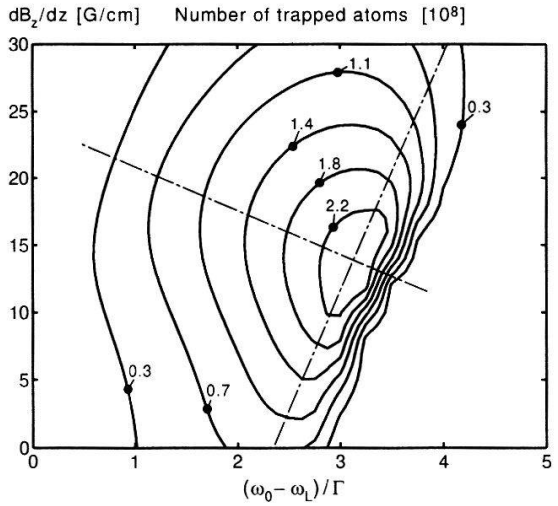

FIG. 4. Calculated contours of equal number of atoms show a much stronger decrease with increasing detuning than is experimentally observed. The theoretical model also predicts captured atoms at zero magnetic field gardient.

This work acknowledges financial support from the Swiss Federal Institute of Technology.

References

[1] K. Lindquist, M. Stephens, and C. Wieman, Phys.Rev. A **46**, 4082 (1992).

[2] C. Monroe, W. Swann, H. Robinson, and C. Wieman, Phys. Rev. A **65**, 1571 (1990).

[3] N. Sagna, G. Dudle and P. Thomann, J. Phys. B: At. Mol. Opt. Phys. **28**, 3213 (1995).

[4] T.W. Hänsch and A.L. Schawlow, Optics Commun. **13**, 68 (1975).

Helv Phys Acta
Vol. 69, Separanda 2 (1996)

0018-0238/96/0200S41-02$1.50+0.20/0

Effect of Noise on Transitions from Chaos to a Steady State

F. Gassmann

General Energy Research, Paul Scherrer Institute, 5232 Villigen PSI

A semi-discrete model system with 14 phase space dimensions approximately simulating a Lorenzian water wheel has been used to investigate the influence of stochastic noise on the lifetimes of chaotic transients. In this study we focus on transitions from chaos to a steady state with indifferent stability. For the first time, a significant shortening by a factor of 3 of mean transition times at a critical noise amplitude could be detected with a nonlinear dynamical system. Surprisingly, the model system can find the delicate steady state much quicker when a stochastic torque noise is added. The effect results from a noise induced modification of the attraction basin of the steady state rather than from affecting the chaotic orbits before the chaos-order transitions occur.

Complex systems often show ordered stationary or periodic states after a shorter or longer chaotic transient when initialized at random. As stochastic environmental or internal noise is always present in natural systems, the combined effect of chaos and stochastic noise determining the time needed for the system to "find" an ordered state is of interest. Up to now much work has been devoted to investigations of noise-induced transitions from a given stationary state over a barrier to another stationary state. More recently, theoretical and experimental studies dealt with noise-induced escape from basins of different types of attractors of dissipative, non-linear dynamical systems far from equilibrium. In contrast to these investigations, we are interested here in noise dependency of transitions from chaos to a steady state. Franaszek [1] showed for the logistic map and the Hénon map that chaotic evolution may be elongated by a maximum of about 20% when small amplitude noise is added and shortened with noise of larger amplitude. However, Blackburn, Grønbech-Jensen, and Smith [2] found no noise dependency for a mathematical pendulum with its point of suspension subjected to a harmonic vertical displacement, neither in simulations nor experimentally with an electronic analog. Also, recent investigations by Lai [3] with a diffusively coupled logistic map lattice revealed only a negligible effect for this 20 dimensional spacio-temporal system. Based on these results he concludes that "the presence of noise is not advantageous in attempts to reduce the transient lifetime".

We describe here results based on numerical simulations of a Lorenzian water wheel with 12 buckets and thus 14 phase space dimensions that was inspired by the techno-scientific masterpiece exhibited at the Technorama in Winterthur. This water wheel was used for testing the numerical model based on the following equations approximately describing the real system:

$$\dot{\varphi} = \omega \quad , \quad \dot{\omega} = \frac{\sum_{i=0}^{n-1} \nu_i \sin\left(\varphi + \frac{2\pi i}{n}\right)}{\tau^2} - \frac{\omega}{\tau_2} + \sigma\xi \quad , \quad \dot{\nu}_i = \frac{\delta_i}{\tau_o} - \frac{1}{\tau_1} \quad , \quad 0 \le \nu_i \le 1$$

The system consists of n (here n = 12) buckets spaced equally around the rim of a wheel rotating around a horizontal axis. The top bucket fills when passing under the faucet ($\delta_i = 1$) that delivers water at a steady rate. The buckets leak steadily and a friction proportional to angular

velocity ω dissipates energy. One arbitrarily chosen bucket defines the angular position φ and ν_i is the normalized water content in bucket i. Key parameters of the system are the time constants τ_o, τ_1 and τ_2 signifying the time for an empty bucket to be filled, the time for a full one to get empty and the friction time constant (set to 1.8 s) respectively. A last parameter $1/\tau^2$ is the maximum angular acceleration exerted from a single full bucket and disappears when time is normalized to τ. Noise is coupled to the system as additive torque noise. σ stands for its amplitude and ξ are numbers from a pseudo random generator with homogeneous distribution on the interval [-1,1]. A new random number is used for every time step Δt set to 0.2 s.

Fig. 1 shows the results of 6 series of 10'000 randomly initialized transients quickly approaching the chaotic attractor. A maximum of 200'000 time steps were calculated for each transient. Transition times to ordered states (steady state or stationary rotation) were statistically analyzed and found to be exponentially distributed analogous to radioactive decay statistics [1,2,4]. To our knowledge, such relevant shortening of mean transition times to an ordered state by a factor of 3 is reported here for the first time. The fact that the transients ended in a fragile steady state with indifferent stability adds to the surprise of the observed noise-induced acceleration of the chaos-order transitions. At noise amplitudes exceeding 0.001 s^{-2} a sharp increase of mean transition times arises from noise-induced escape from the steady state back to the chaotic attractor and can be described by a Arrhenius relation. Inspection of many transitions by a method described in detail in [4] shows that the novel noise effect cannot be understood as a noise-induced escape from the chaotic attractor but rather as a noise-induced trapping of the chaotic trajectories by a probabilistic basin of the attractor for the steady state. As we are interested in the study of complex systems rather than in an accurate simulation of the Lorenzian water wheel, serving only as a physical guideline, the dependence of the effect on the time step and on numerical simplifications (Euler integration, φ is integer in the range [-10'000, 10'000], sine table with increments of $2\pi/2048$) is not considered as a disadvantage. In addition, we show in [4] a shortening of chaos lifetime exceeding 4 decades (investigating transitions to the stationary rotation) not depending on the time step and so proving the physical reality of the novel phenomenon. The here reported noise-catalyzed spontaneous emergence of order out of chaos is clearly different from the well known stochastic resonance and its potential implications might cover diverse research areas dealing with complex multistable systems subjected to noise [4].

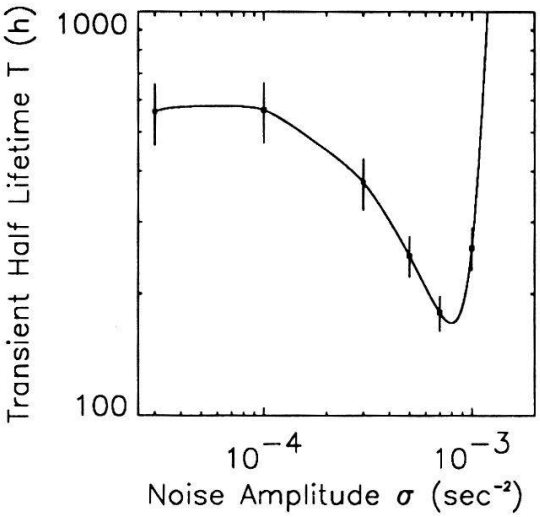

Fig. 1. Noise dependency of transition times from chaos to a steady state for $\tau_o = 1.44$ s, $\tau_1 = 10$ s. Error bars indicate ± twice the standard deviation.

References

[1] M. Franaszek, Phys. Rev. A **44**, 4065 (1991).
[2] J.A. Blackburn, N. Grønbech-Jensen, and H.J.T. Smith, Phys. Rev. Lett. **74**, 908 (1995).
[3] Y.C. Lai, Phys. Letters A **200**, 418 (1995).
[4] F. Gassmann, submitted to Phys. Rev. E.

Helv Phys Acta
Vol. 69, Separanda 2 (1996)

0018-0238/96/0200S43-02$1.50+0.20/0

A NON-LOCAL METHOD LEADING TO THE DIFFERENCE-QUOTIENT TURBULENCE MODEL

P.W. Egolf
Swiss Federal Laboratories for Materials Testing and Research, CH-8600 Dübendorf

D.A. Weiss
Laboratoire PMMH, École Supérieure de Physique et de Chimie Industrielles de la Ville de Paris, F-75231 Paris, France

Based on ideas of Prandtl, Hinze proposed to describe turbulence properties - e.g. the Reynold's shear stress - as those of a visco-elastic fluid, including a description of memory behaviour. For the time-averaged quantities of a quasi-stationary flow an analogous non-local approach can be formulated. From this, by assuming a perfect coherence over a well defined distance, the difference-quotient turbulence model has been obtained.

When deriving from the Navier Stokes equations the Reynold's equations, containing time-averaged values, second order moments appear. Further equations can be established to solve the problem also containing these second order moments. But then again one order higher correlation's - now third order moments - sneak into the expanding system of equations. Continuing, in the end one has to solve a set of infinite partial differential equations. - It is known, that in special cases, maybe because of occurring scaling properties, such a set can be replaced by one equation only, with a dependence on the lowest order moment, but now showing a nonlocality. Such a transformation of the equations is equivalent to the closure technique, well-known in the theory of turbulence.

The obvious insufficiency of local gradient-type turbulence transport was noticed by Corrsin [1] and more recently by Bernard & Handler [2]. Based on investigations of Rivlin [3], Hinze [4] proposed to introduce a generalization analogously to a description of visco-elastic fluids, by including a memory behavior $\tilde{M}(t)$ depending on the time variable t

$$\overline{u'_2 u'_1} = -\left(\frac{\varepsilon}{\rho}\right) \cdot \int_0^\infty d\tau \cdot \tilde{M}(\tau) \cdot \left[\frac{\partial \bar{u}_1}{\partial x_2}(t-\tau) + \frac{\partial \bar{u}_2}{\partial x_1}(t-\tau)\right], \qquad \varepsilon \propto \chi_2 \cdot \bar{u}_1 . \tag{1}$$

In equation (1) the modified eddy viscosity ε is directly proportional to a length scale χ_2 and the time-averaged velocity difference in the main flow direction - described by co-ordinates x_1 - of a turbulent shear flow, here generalized to be $(\bar{u}_1 - \bar{u}_{1_{min}})$. It is known that memory effects in time are the analog to nonlocalities in "real" space. Because at the moment, we are only considering quasi-stationary cases, it may seem useful to study equation (1) in Euclidean space by replacing the time t by the transverse co-ordinate x_2 and the memory function $\tilde{M}(t)$ by a corresponding non-local function $\tilde{N}(x_2')$

$$\overline{u'_2 u'_1} = -\sigma \cdot \chi_2 \cdot (\bar{u}_1 - \bar{u}_{1_{min}}) \cdot \int_{-\infty}^{\infty} dx_2' \cdot \tilde{N}(x_2') \cdot \frac{\partial \bar{u}_1}{\partial x_2}(x_2 - x_2'). \tag{2}$$

The constant σ depends on the turbulence intensity. The space co-ordinate difference guarantees Galilean invariance. In equation (2) the assumption of a flow with a large velocity gradient that is transverse to the direction of the main flow is considered, so that this gradient is at least one order larger than the gradient in the perpendicular direction with reversed indices. Therefore the smaller gradient has been neglected. The nonlocality can also be considered as due to a probability density function for the effectiveness of eddies with different correlation lengths, respectively corresponding radii. Therefore we rewrite (2) to obtain

$$\overline{u'_2 u'_1} = -\sigma \cdot \chi_2 \cdot (\bar{u}_1 - \bar{u}_{1_{min}}) \cdot \frac{\int_{-\infty}^{\infty} dx_2' \cdot N(x_2') \cdot \frac{\partial \bar{u}_1}{\partial x_2}(x_2 - x_2')}{\int_{-\infty}^{\infty} dx_2' \cdot N(x_2')}. \tag{3}$$

The considered normalized nonlocality function $\tilde{N}$ has now been replaced by a non-normalized counterpart N. It is a characteristic function and can be described by a linear combination of Heaviside distributions (two-sided step 'functions'). The quantity $\lambda = x_{2_{max}} - x_2$ is a correlation length. Then it follows

$$N = \begin{cases} 0, & x_2' < x_2 \\ 1, & x_2 \le x_2' \le x_2 + \lambda \\ 0, & x_2 + \lambda < x_2'. \end{cases} \Rightarrow \overline{u'_2 u'_1} = -\sigma \cdot \chi_2 \cdot (\bar{u}_1 - \bar{u}_{1_{min}}) \cdot \frac{\int_{x_2}^{x_{2_{max}}} dx_2' \frac{\partial \bar{u}_1}{\partial x_2}(x_2')}{\int_{x_2}^{x_{2_{max}}} dx_2'}. \tag{4a,b}$$

It is known that in many turbulent flows - because of self-similarity - the mean velocity in the main flow direction can be separated in order of the two variables x_1 and x_2. Therefore, with this assumption, the right-hand side of equation (4b) can be integrated. This leads to the *difference-quotient turbulence model* [5], which has been developed by completely other means ($x_{2_{max}} := \{x_2 | \bar{u}_1 = \max_{x_2}\{\bar{u}_1\}\}$.

$$\overline{u_2' u_1'}(x_1, x_2) = -\sigma \cdot \chi_2 \cdot \left[\bar{u}_1(x_1, x_2) - \bar{u}_{1_{min}}(x_1)\right] \cdot \frac{\bar{u}_{1_{max}}(x_1) - \bar{u}_1(x_1, x_2)}{x_{2_{max}} - x_2}. \tag{5}$$

[1] S. Corrsin, Adv. Geophysics **18 A**, 25-60 (1974).
[2] P.S. Bernard & R.A. Handler, J. Fluid Mech. **220**, 99-124 (1990).
[3] R.S. Rivlin, Quart. Appl. Math. **15**, 212-215 (1957).
[4] J.O. Hinze, *Turbulence*, 2nd ed., Mac Graw-Hill, New York (1975).
[5] P.W. Egolf, Phys. Rev. E **49 (2)**, 1260-1268 (1994).

Helv Phys Acta
Vol. 69, Separanda 2 (1996)

0018-0238/96/0200S45-02$1.50+0.20/0

ANALYTICAL REYNOLD'S STRESSES OF AXI-SYMMETRIC JETS

P.W. Egolf
Swiss Federal Laboratories for Materials Testing and Research, CH-8600 Dübendorf

D.A. Weiss
Laboratoire PMMH, École Supérieure de Physique et de Chimie Industrielles de la Ville de Paris, F-75231 Paris Cedex 05, France

The difference-quotient turbulence model, describing the Reynold's shear stress of an axi-symmetric jet, has now been modified to relate to the normal stress in the main flow direction. The simple analytical results show, that in an experiment self-preservation has not been achieved completely. A proposition of the theory states, that a relative turbulence intensity is just equal to the square root of the spreading parameter of the jet. This result is confirmed by experimental data.

The difference-quotient turbulence model, which was applied to solve some problems of the axi-symmetric jet, was published in 1994 [1]. For the Reynold's shear stress $\overline{u'_2 u'_1}$, in a self-similarity domain ($x_1 >> x_0$), an analytical function has been derived, which describes experimental data very convincingly. - In this article, the aim is to concentrate on the normal turbulence stress in the main flow direction, with co-ordinates x_1. By a replacement of all second indices by the first one (2—>1) in the difference-quotient turbulence model, the following second order symmetric correlation function is obtained

$$\overline{u'^2_1} = -\sigma \cdot \chi_1 \cdot \left(\overline{u}_1 - \overline{u}_{1_{min}}\right) \cdot \frac{\overline{u}_{1_{max}} - \overline{u}_1}{x_{1_{max}} - x_1}, \qquad \sigma = \beta . \tag{1a,b}$$

Then the following obvious relations (compare with solutions in Ref. [1])

$$\overline{u}_{1_{min}} = 0, \quad \overline{u}_{1_{max}} = u_0, \quad \overline{u}_1 = u_0 \cdot \left(\frac{x_0}{x_1}\right) \cdot f, \quad f = \exp\left[-\frac{1}{2}\left(\frac{x_2}{\beta \cdot x_1}\right)^2\right], \quad x_{1_{max}} = x_0, \tag{2a-e}$$

and the length scale χ_1 - which is identical to the only characteristic length in the main flow direction, the core distance x_0 - are substituted into equation (1a). After some small rearrangements the following equation is obtained

$$\frac{\overline{u'^2_1}}{\overline{u_1}(0)^2} = \beta \cdot \frac{\frac{x_1}{x_0} - f}{\frac{x_1}{x_0} - 1} \cdot f, \qquad \overline{u_1}(0) := \overline{u_1}(x_1, x_2)\big|_{x_2=0} = u_0 \cdot \left(\frac{x_0}{x_1}\right). \tag{3a-c}$$

For a spreading parameter of the jet β=0.082 - by taking equation (3a) into consideration - the normal stresses were calculated (Fig. 2). Analogous calculations with β=0.062 are compared with experimental data from Ref. [3] (see Fig. 3).

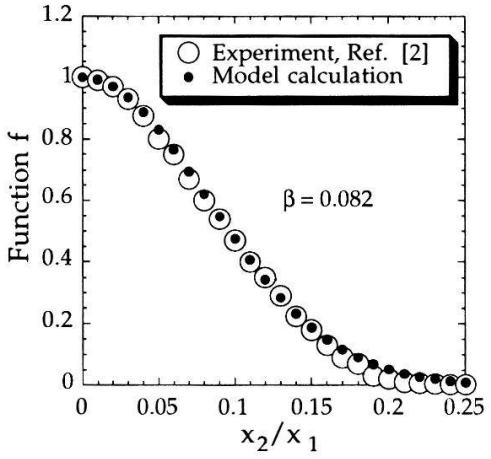

Figure 1: The function f obtained in Ref. [1] is compared with a least-squares spline fit to the experimental data of Ref. [2].

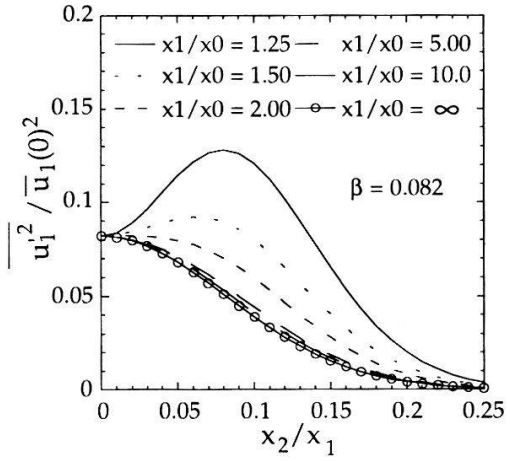

Figure 2: The normal Reynold's stress for different distances x_1/x_0. The quantity x_0 denotes the core distance of the jet.

From (3a) it follows immediately

$$\Omega_{x_1/x_0} := \left(\frac{\frac{x_1}{x_0} - 1}{\frac{x_1}{x_0} - f} \right) \cdot \frac{1}{f} \cdot \left(\frac{\overline{u_1'^2}}{\overline{u}_1(0)^2} \right) = \Omega = \beta = \text{constant}, \qquad \forall \left(\frac{x_1}{x_0} \right). \tag{4a-d}$$

An already "proven" proposition (P) can be stated: ***The scaled relative fluctuation intensity $\sqrt{\Omega}$ is constant and equal to the square root of the spreading parameter of the jet $\sqrt{\beta}$.*** Measured data of Ref. [3] presented in Fig. 4 confirm (P).

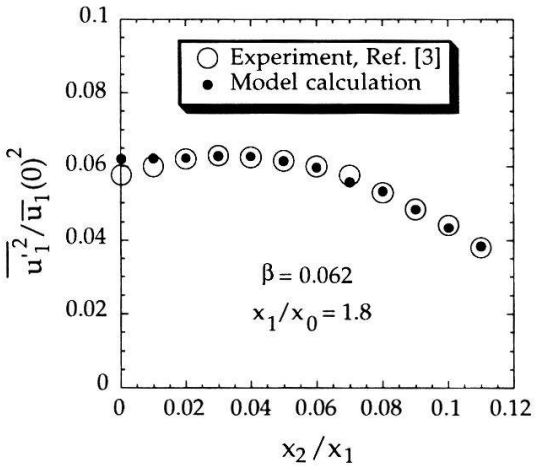

Figure 3: The theoretically predicted maximum of the partial kinetic fluctuation energy at $x_1/x_2 > 0$ for x_1/x_0 small (see Fig. 2) is clearly represented by measurements (Ref. [3]).

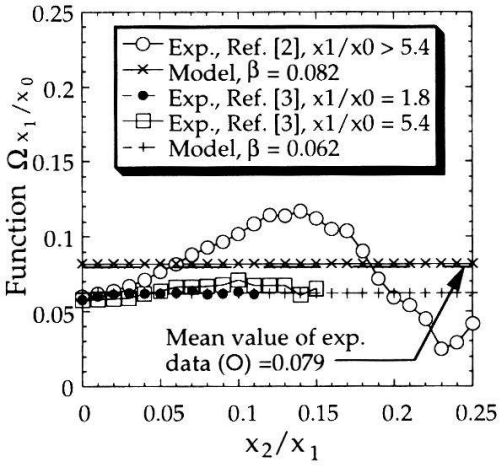

Figure 4: Ω is very useful to test theoretical results with experimental data. The measurements presented in Ref. [3] confirm the calculated results in a convincing manner.

[1] P.W. Egolf, Phys. Rev. E **49 (2)**, 1260-1268 (1994).
[2] N.R. Panchapakesan and J.L. Lumley, J. Fluid Mech. **246**, 197-223 (1993).
[3] I. Wygnanski and H. Fiedler, J. Fluid Mech. **38** (3), 577-612 (1969).

Helv Phys Acta
Vol. 69, Separanda 2 (1996)

0018-0238/96/0200S47-02$1.50+0.20/0

A Method to Determine the Tumor Position during Radiation Treatment

S. Kirsch, H.U. Boksberger, U. Greuter,
C. Schilling, and P.G. Seiler

Paul Scherrer Institut, 5232 Villigen PSI, Switzerland

Modern irradiation techniques (e.g. proton therapy) allow for the applied radiation dose to be tailored to the three dimensional shape of the tumor. In these techniques it is assumed that the tumor position remains constant over the treatment time. However, many tumors move, especially in the chest and abdomen region. A method has been developed, which can detect the position of a magnetic dipole (miniaturized coil) in real time, which has been previously implanted or inserted at the tumor. The results of this position determination can be used to interrupt the treatment or adjust the beam position, if the tumor is not within the target area.

Radiation treatment is one of the main techniques used to cure cancer. The goal is to destroy all the tumor cells by applying a lethal radiation dose to the tumor and at the same time keep the dose in the healthy tissue as low as possible. These two opposite requirements can be achieved by tailoring the dose distribution to the three dimensional shape of the tumor (conformal radio therapy). However, many tumors, especially in the chest and the abdomen, move and therefore distort the precision of dose application to the patient. Here a method is proposed, which can determine the position of the tumor within the patients body in real time. When the position of the tumor is known, the treatment can be interrupted or the beam position can be adjusted if the tumor moves outside of the target area.

A miniaturized coil will be implanted or inserted such that it is connected to the tumor and moves with it. The implantation can be performed with puncture needles. This magnetic dipole is connected to a signal generator outside the body. It emits a slowly modulated (quasi-static) magnetic dipole field, which is described by:

$$\vec{H}(\vec{r}_d - \vec{r}_c, \vec{m}) = \frac{3\,[\vec{m}(\vec{r}_d - \vec{r}_c)]\,(\vec{r}_d - \vec{r}_c)}{|\vec{r}_d - \vec{r}_c|^5} - \frac{\vec{m}}{|\vec{r}_d - \vec{r}_c|^3}\ ,$$

where $\vec{r}_d$ and $\vec{r}_c$ are the position of the dipole and the point where the magnetic field is measured, respectively. $\vec{m}$ denotes the magnetic moment of the dipole. The dipole field is modulated with a frequency of less than 10 kHz. In this frequency region, the magnetic field is practically unaffected by the human body. Therefore the dipole position can be derived from magnetic field measurements with sensors outside the body.
According to [1], induction coils are best suited as magnetic field sensors for this frequency and magnetic field strength region. The induced signal is proportional to the mean value of the magnetic field strength within the coil volume. We have chosen the coil length L

according to:

$$L = r_o \frac{3}{\sqrt{5}} \sqrt{\frac{1-(\frac{r_i}{r_o})^5}{1-(\frac{r_i}{r_o})^3}} ,$$

where r_i and r_o are the first and last wire layer radius, respectively. In this case the induced signal corresponds approximately to the magnetic field strength in the coil center [2]. This simplifies the algorithm to determine the dipole position substantially. Two axially displaced induction coils form a gradiometer.
The gradiometer signals are less than 100 μV and therefore have to be amplified by a low noise amplifier. Since we are working in a noisy environment, several measures are taken to extract the signal from the background. The gradiometer itself improves the noise rejection compared to a single coil, because only a voltage difference is measured. Therefore distant noise sources with their low field derivatives are further suppressed with respect to the local dipole field. Furthermore, the signal is filtered by an active bandpass tuned to its frequency. After signal digitization, Fourier analysis and the precise knowledge of the generated dipole signal are used to determine the signal amplitude and phase, which are related to the value and sign of the magnetic field.
To evaluate a dipole position in space one has to determine its coordinates $\vec{r}_d = [x_d, y_d, z_d]$ and the direction of its moment $\vec{m} = m[\cos\phi_d \sin\theta_d, \sin\phi_d \sin\theta_d, \cos\theta_d]$. Assuming the absolute magnetic moment m is known, it is shown in [3] that by measuring five linear independent derivatives of the magnetic field at one space point, the position of the dipole can be evaluated within a fourfold ambiguity, and this must be resolved by a priori knowledge. Inspired by [3] we designed an array of the form of a tetrahedron, where on each axis an induction coil gradiometer is placed. Because of the size and the arrangement of the gradiometers a measurement of the derivatives at one space point is impossible. Therefore the dipole position is determined by an iterative procedure, where its position parameters are varied to minimize the χ^2 of the measured gradiometer voltages and their theoretical predictions for a given dipole position.

First measurements with a prototype tetrahedron array where performed. With the dipole up to 40 cm away from the outer edge of the tetrahedron array, which corresponds to a clinical situation, its position can be determined with an uncertainty of $\sigma_{x,y,z} = 2-3$ mm in all three coordinates. The uncertainty of the dipole direction is $\sigma_{\phi,\theta} < 15$ mrad.

The authors thank H. Blattmann, G. Munkel and E. Pedroni from the department of radiation medicine at PSI for continuous support and many fruitful discussion and T. Lomax for careful reading the manuscript.

References

[1] R. Boll and K. J. Overshott (Eds.), *Magnetic Sensors*, Weinheim: VCH, 1989.

[2] H. Zijlstra, *Experimental methods in Magnetism*, Amsterdam: North-Holland, 1967.

[3] W. M. Wynn et al., IEEE Trans. Mag. 1975, MAG-11, 701-707.

Helv Phys Acta
Vol. 69, Separanda 2 (1996)

0018-0238/96/0200S49-02$1.50+0.20/0

Solar Corona Diagnostic with Solar Wind Iron Charge Spectra

M.R. Aellig[1], H. Grünwaldt[2], S. Hefti[1], P. Wurz[1], P. Bochsler[1], W.I. Axford[2], H. Balsiger[1], A. Bürgi[6], M.A. Coplan[3], A.B. Galvin[3], J. Geiss[4], F. Gliem[5], G. Gloeckler[3], M. Hilchenbach[6], D. Hovestadt[6], K.C. Hsieh[7], F.M. Ipavich[3], D.L. Judge[8], R. Kallenbach[1], B. Klecker[6], M.A. Lee[9], S. Livi[2], G.G. Managadze[10], E. Marsch[2], E. Möbius[9], M. Neugebauer[11], H.S. Ogawa[8], K.U. Reiche[5], M. Scholer[6], M.I. Verigin[10], B. Wilken[2]

(1) Physikalisches Institut, University of Bern, CH-3012 Bern, Switzerland
(2) Max-Planck-Institut für Aeronomie, D-37189 Katlenburg-Lindau, Germany
(3) Dept. of Physics and Astronomy, University of Maryland, College Park, MD 20742, USA
(4) International Space Science Institute, CH-3012 Bern, Switzerland
(5) Institut für Datenverarbeitung, Technische Universität, D-38023 Braunschweig, Germany
(6) Max-Planck-Institut für extraterrestrische Physik, D-85740, Garching, Germany
(7) Dept. of Physics, University of Arizona, Tucson, AZ 85721, USA
(8) Space Science Center, University of Southern California, Los Angeles, CA 90089, USA
(9) EOS, University of New Hampshire, Durham, NH 03824, USA
(10) Institute for Space Physics, Moscow, Russia
(11) Jet Propulsion Laboratory, Pasadena, CA 91103, USA

Matter flowing away from the solar surface becomes highly ionized in the corona ($T \approx 2 \cdot 10^6 K$) by collisions with electrons. Due to the decreasing electron density with increasing distance from the solar surface, the charge state distributions freeze and remain unaltered throughout the interplanetary medium. This is why charge spectra measured at 1 AU are a valuable diagnostic tool for temperature and density variations in the inner solar corona. Preliminary results of iron charge spectra obtained from the SOHO CELIAS CTOF mass spectrometer indicate a patchy structure of the corona at scales of $\approx 10^4$ km.

One open issue in solar physics is the problem of coronal heating, i.e., the question, why the solar corona, the uppermost part of the solar atmosphere, is more than two orders of magnitude hotter than the photosphere, i.e., the visible surface of the sun, and how this elevated temperature is maintained.

The CELIAS experiment [1] onboard SOHO consists of three mass spectrometers to analyze the minor ions in the solar wind — a plasma composed of protons (96%), alpha particles (4%), and of minor ions (e.g. C, O, Fe) — that flows away from the sun. The linear time-of-flight mass spectrometer CTOF allows to unambiguously determine mass, ionic charge and energy of every particle entering the instrument.

Matter upstreaming from the photosphere becomes ionized by collisions with electrons as it

passes the chromosphere and moves into the hot corona. The density of the charge state $i+$ of a the species X is given by

$$\frac{dn_i}{dt} = n_e[n_{i-1}C_{i-1} - n_i(C_i + R_i) + n_{i+1}R_{i+1}] \quad (1)$$

where C_i and R_i denote the highly temperature dependent ionization and recombination rate coefficients of X^{i+}, and n_e and n_i the densities of electrons and of X^{i+}, respectively. When the charge exchange time between two adjacent ionization levels equals the solar wind expansion time, i.e., the time it takes a particle to pass one electron density scale height, the momentary populations of the two ionization stages are frozen and remain unaltered on the particles way into interplanetary space. Freezing-in of a pair X^{i+}, X^{i+1+} occurs at an electron density $n_{f,i} \propto \frac{1}{\sqrt{C_i+R_{i+1}}}$. Each pair freezes at a different electron density and, correspondingly, at a different electron temperature. Unlike the density and solar wind velocity, the relative population of the ionization levels does not change from the freeze-in point to the SOHO spacecraft near the earth's orbit. Thus charge spectra carry information about the conditions in the lower corona and provide a powerful tool for coronal diagnostic by remote sensing. Spatial variations both in electron density and temperature in the corona translate into temporal variations of the freeze-in temperatures due to the rotation of the sun.

Freeze-in temperatures in the solar wind are derived from abundance ratios of adjacent ionization levels of the same species, assuming an equilibrium between the two stages. The temperatures determined from three pairs of iron ions are shown in Fig. 1. They were calculated with the maximum time resolution of five minutes, which was never reached in solar wind measurements before, and then smoothed with a boxcar average of 25 minutes width.

The three temperatures show a collective behaviour with time, but their absolute value is different, which demonstrates, that freezing-in occurs at different electron densities and thus at different temperatures for each ion pair. The pairs with lower i freeze at lower electron density, because the reaction rates decrease from Fe^{9+} to Fe^{12+}. Since the calculated temperature of the ratio of Fe^{10+}/Fe^{9+} is lower than the other ones, we conclude that freezing-in occurs outwards of the electron temperature maximum in the corona.

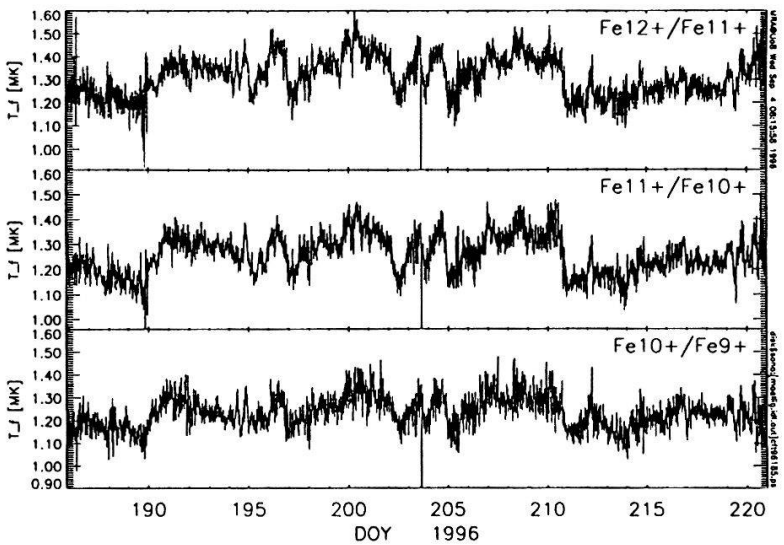

Fig. 1: Iron freeze-in temperatures.

Shortscaled variations with the typical duration of hours can be identified from these spectra and, together with the steep gradients observed, they reveal the very patchy structure of the corona, which is conserved througout the solar wind acceleration process.

References

[1] D. Hovestadt et al., Solar Physics **162**, (1995) 441-481.